PCCP

Exploring the Biointerfaces: Ab Initio Investigation of Nano-Montmorillonite Clay, and its Interaction with Unnatural Amino Acids

Journal:	*Physical Chemistry Chemical Physics*
Manuscript ID	CP-ART-06-2023-002944.R1
Article Type:	Paper
Date Submitted by the Author:	18-Sep-2023
Complete List of Authors:	Fernando, Warnakulasuriya Ashan; University of North Dakota Khan, Desmond; University of North Dakota Hoffmann, Mark; University of North Dakota, Cakir, Deniz; University of North Dakota

PCCP

ARTICLE TYPE

Cite this: DOI: 00.0000/xxxxxxxxxx

Exploring the Biointerfaces: Ab Initio Investigation of Nano-Montmorillonite Clay, and its Interaction with Unnatural Amino Acids†

Ashan Fernando,[a] Desmond Khan,[b] Mark R. Hoffmann,[b] and Deniz Çakır [a]

Received Date
Accepted Date

DOI: 00.0000/xxxxxxxxxx

We investigated the interaction between biomimetic Fe and Mg co-doped montmorillonite nanoclay and eleven unnatural amino acids. Employing three different functionals (PBE-GGA, PBE-GGA+U, and HSE06), we examined the clay's structural, electronic, and magnetic properties. Our results revealed the necessity of using PBE-GGA+U with U $\geq$ 4 eV to accurately describe key clay properties. We identified amino acids that strongly interacted with the clay surface, with steric orientation playing a crucial role in facilitating binding. Our DFT calculations highlighted significant electrostatic interactions between the amino acids and the clay slab, with the amino group's predominant role in this interaction. These findings hold promise for designing amino acids for clay-amino acid systems, leading to innovative bio-material composites for various applications. Additionally, our ab-initio molecular dynamics simulations confirmed the stability of clay-amino acid systems under ambient conditions, and the introduction of an implicit water solvent enhanced the binding energy of amino acids on the clay surface.

1 Introduction

Human bone tissues play a crucial role in supporting the body's functionality, including locomotion, tissue protection, and housing the bone marrow responsible for blood cell production[1]. While bone tissues possess the ability to self-heal over time, this regenerative capacity may be impaired or diminished in certain individuals, leading to complications and hindering tissue regrowth. Additionally, severe bone injuries often necessitate medical intervention as they may not heal naturally within a reasonable time frame. Consequently, there is a need to explore artificial methods to promote bone tissue regeneration through various strategies[2]. Moreover, the engineering of artificial bone tissues can contribute to the development of biological models facilitating the understanding and treatment of cancerous tumors originating in or migrating to the bone marrow[3].

In the pursuit of creating an artificial bone tissue environment, nanocomposite biomaterial systems have emerged as crucial components[4,5]. Tissue engineering, an interdisciplinary field, focuses on developing biocompatible materials with appropriate mechanical properties to facilitate tissue regeneration. Porous three-dimensional scaffolds play a pivotal role in tissue engineering by providing an optimal microenvironment for tissue and organ regeneration. Composite systems combining polymers and nanoscale fillers have been developed to achieve biocompatibility, biodegradability, and desirable mechanical properties for tissue engineering applications[6–9]. Polymer-based nanocomposites, including polymer/clay nanocomposites (PCNs), exhibit enhanced mechanical strength[10,11], thermal stability[12], reduced gas permeability[13] and ionic conductivity[14], and biodegradability[15]. Montmorillonite (MMT) clay, a layered silicate, significantly influences PCNs by enhancing their thermal properties, elastic modulus, and hardness[16]. The modification of clay affects the properties of nanocomposites, and molecular dynamics simulations have highlighted the importance of interactions between polymers, clay, and organic modifiers in terms of crystallinity and nanomechanical characteristics of PCNs[17]. MMT clay also possesses therapeutic qualities such as toxin adsorption, making it suitable for structural applications in bone tissue engineering biomaterials. Simulation studies have demonstrated the interaction between nanoclay and amino acids, suggesting the use of synthetic and biocompatible amino acids for clay modification. Previous research has shown that modifying clay galleries with unnatural amino acids enhances osteogenesis and bone growth[18–20]. Therefore, the use of polymer-based nanocomposites, including PCNs, represents a promising avenue for developing new materials with improved properties for tissue engineering applications.[21–32]

In our study, we utilized a nanocomposite system to mimic the bone tissue environment, which consists of nano MMT clay co-

[a] Department of Physics and Astrophysics, University of North Dakota, Grand Forks, North Dakota 58202, USA; E-mail: deniz.cakir@und.edu
[b] Department of Chemistry, University of North Dakota, Grand Forks, North Dakota 58202, USA

doped with Fe and Mg. This clay, with the chemical formula $NaSi_{16}(Al_6FeMg)O_{20}(OH)_4$, exhibits negative charge states resulting from the isomorphic substitution of Al by Mg and Fe in MMT. The compensatory insertion of Na^+ ions between the clay layers helps balance the negative charge. Montmorillonite is a naturally occurring clay mineral belonging to the smectite group[33]. It consists of H, O, Si, Al, Mg, and Fe atoms arranged in two tetrahedral sheets and one octahedral sheet, with space between the triple-sheet layers[21,34]. A model for the mechanical behavior of Na-Montmorillonite clay[22] along with some first-principle studies conducted previously, provide valuable insight when examining the optical, structural, and electronic properties of transition metal-doped MMT[23,24] and Kaolinite[25] clay surfaces. Understanding the atomic-scale behavior of the montmorillonite clay surface is crucial due to its chemical properties, which enable the intercalation of organic molecules such as amino acids[26]. This characteristic offers the potential to develop biomaterial nanocomposite systems that replicate the properties of human bone tissues. Therefore, investigating the interactions between the clay surface and amino acids at an atomic level becomes essential. Furthermore, identifying the amino acids that best complement the clay surface to create such an environment is crucial, as highlighted in previous studies[27–32]. Amino acids with a high binding energy to the clay surface are particularly desirable in this context. In order to investigate the interaction between biomimetic Fe and Mg co-doped montmorillonite nanoclay and a variety of unnatural amino acids, we conducted a density functional theory study utilizing eleven distinct structures of unnatural amino acids. The utilization of unnatural amino acids offers two significant advantages: it expands the range of accessible chemical and physical properties beyond those found in natural amino acids, and it minimizes interference with protein synthesis compared to their natural counterparts. Among the factors affecting the suitability of bioengineered bone replacements are the effects, both beneficial and detrimental, of metal ions. Most studies have focused on medical outcomes or structural properties. Still, many of the details (i.e. atomic level) of the functioning of such bioengineered bone replacements are not fully understood. This is particularly the case for details of their electronic structure. This manuscript elucidates one particular aspect of the interaction of unnatural amino acids, which have been suggested and used for bioengineered bone replacements, with doped clays[35,36].

2 Computational details

Throughout this study, we used Density Functional Theory (DFT) calculations[37,38] as implemented in Vienna *ab*-initio Simulation Package (VASP)[39–41]. The electron-ion interactions were described by employing a projected augmented wave (PAW) method[42,43] with an energy cutoff value of 500 eV. The exchange-correlation functional called Generalized Gradient Approximation of Perdew, Burke, and Ernzerhof (PBE–GGA)[44] was employed with and without a Hubbard U correction to accomplish a correct description of *d*-electrons of the Fe atom[45]. The appropriate U parameter for an atom depends on its chemical environment, and therefore it should be carefully determined. We found that a U value of between 4.0 - 5.0 eV yields an accurate description of the Fe atoms[46] embedded into the clay slab. Moreover, we also utilized the Heyd-Scuseria-Ernzerhof (HSE06) hybrid functional[47,48] to validate the accuracy of our GGA+U calculations. The HSE06 functional is widely recognized for its accuracy and precision, making it a reliable standard for comparing the properties predicted by the PBE and PBE-D3 functionals. HSE06 incorporates a fraction of Hartree-Fock exchange, which improves its accuracy in predicting electronic properties such as band gaps, which are often challenging for pure GGA functionals like PBE to reproduce accurately. In a recent work, the band gap, calculated using HSE06, for Fe^{2+} doped sodium montmorillonite clay equals 4.3 eV, demonstrating excellent concurrence with experimental results derived from ultraviolet-visible spectroscopy[24]. DFT+U approach was widely applied for the description of the layer structure and the electronic properties of iron-containing clay minerals.[23,49,50] The energy convergence criterion was set to 10^{-6} eV, while the force convergence criterion of the ionic steps was 10^{-2} eV/Å. A vacuum spacing of 15 Å was set to avoid interaction with the periodic image in the z-direction. Bader charge on the atoms was calculated as a function of the charge state of the clay slab and functional type[51–54]. In addition to neutral clay, we also explored the charged one. The NELECT parameter in the VASP code is used to specify the total number of electrons in the system. By default, VASP calculates this value based on the assumption of charge neutrality within the system. However, if NELECT is set to a different value, indicating a deviation from the default electron count, VASP applies an additional neutralizing background charge to ensure overall charge neutrality in the system. Binding energies of amino acid molecules were also obtained using an implicit water solvent model, for which we used VASPsol[55,56] which incorporates solvation into the VASP code within a self-consistent continuum model. Depending on the size of the amino acid, we utilized either a $2\times2\times1$ or a $3\times2\times1$ clay structure with all layers relaxed along with $3\times3\times1$ or $2\times3\times1$ Monkhorst-Pack[57] k-point meshes for the structure optimizations, respectively. We used much larger k-point meshes for the density of states and charge density calculations. We included van der Waals (vdW) interactions using the DFT-D3 method[58], including Becke-Johnson damping[59]. We also employed first-principles molecular dynamics (AIMD) simulations at 300 K for the selected systems using a Nose-Hoover thermostat[60]. AIMD simulations were conducted under vacuum conditions using a 1 fs time step for a total simulation time of 7.5 ps. Finally, the total dipole moments of amino acids determined in this study involved both gas phase and solvent (water) systems, utilizing the Pople basis set 6-31G* for the molecular orbitals. We employed the HSE06 hybrid functional as a reference to assess the performance of the PBE and PBE-D3 functionals[61]. The basis set consists of 6 Gaussian type orbitals (GTOs) for the inner shell, 3 GTOs for the inner valence, and 1 GTO for the outer valence, along with a set of polarization functions applied to the heavier atoms. These calculations were carried out using Gaussian 09 software, employing a default energy convergence criterion of 10^{-8} eV[62]. We employed Gaussian 09 calculations for solely calculating dipole moments of amino acids. An ultra-fine numerical pruned grid, comprising 99 radial shells and 590 angular points per shell, was utilized, resulting in

approximately 9000 points per atom.

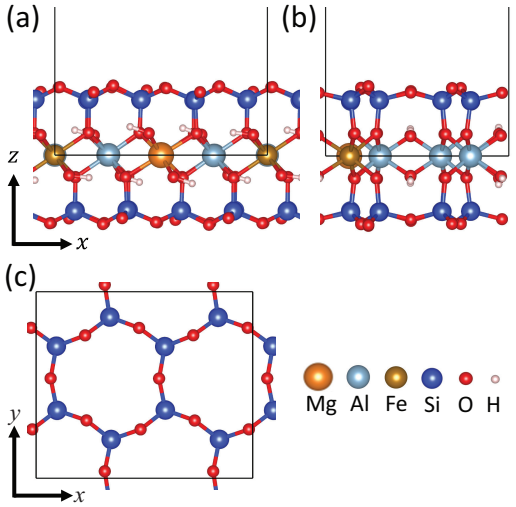

Fig. 1 Side views of clay surface in (a) and (b). The atomic structure of the surface layer is shown in (c).

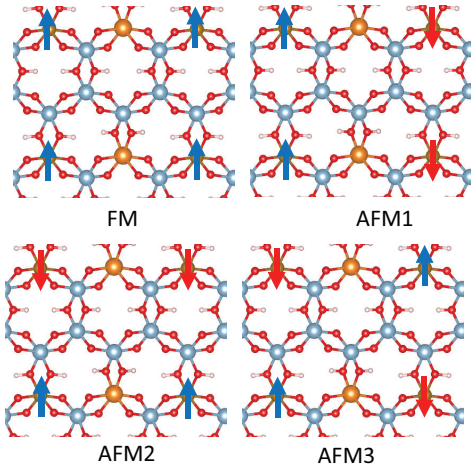

Fig. 2 Ferromagnetic and various antiferromagnetic configurations on a 2×2 supercell structure. We only show the clay layer containing Fe atoms which possess a cis-octahedral coordination, where -OH groups anti-symmetrically bind to Fe. The blue (red) arrow denotes up and down spin.

3 Results and Discussion

3.1 Structural and Magnetic Properties of the Clay Surface

Figure 1 shows the structure of the clay slab where two of the Al atoms in the octahedral sheet are substituted by a Fe and a Mg atom. In other words, the concentrations of dopants (Fe and Mg) are 12.5%. Presence of the Fe atom necessities using functionals beyond GGA-PBE for correct description of localized d orbitals. In this respect, we employed both GGA+U method and HSE06 to provide a better description for the localized d electrons of the Fe atom. We relaxed the atomic positions and lattice parameters of the neutral clay slab using different U values (1-5 eV) and HSE06 functional. The Fe-O and O-H bond lengths were obtained from those relaxed calculations. We observed that O-H bond length ($\sim$ 0.96 Å) remains constant for all U values, which is in agreement with other theoretical results[24,63], but the average distance between Fe and six nearest neighboring O atoms increase from 1.90-1.95 Å to 1.95-2.05 Å as the U value changes from 0 to 5 eV. The Fe-O bond length is the largest for the high-spin state where the magnetic moment per Fe atom is around $4\mu_B$. The Fe-O and O-H bond lengths obtained from U=4 and 5 eV are well consistent with the HSE06 results. Similarly, the lattice parameters are also dependent on the functional and increase as U varies from 0 to 5 eV. U=4 and 5 eV, and HSE06 result in close lattice parameters as seen in Table 1. Substitution of two Al^{3+} ions with one Mg^{2+} and one Fe^{3+} gives rise to a negatively charged clay slab[24]. We assessed the magnetic and electronic structure of the clay slab using both GGA+U and HSE06 functionals with respect to the charged state of the clay slab. We considered neutral, singly, and doubly negatively charged clay. We computed Bader charge and magnetic moment (in the ferromagnetic state which is the ground state spin configuration of the clay slab) on the Fe atom. The Fe atom has an electronic configuration of [Ar]$3d^6 4s^2$. The magnetic moment (charge) on Fe increases as 1.73→1.92→4.08→4.27 μ_B (+1.72→+1.75→+1.91→+1.92 $|e|$) as U changes as 0→2→4→5 eV for the neutral clay slab. When U≥4, the charge on the Fe atom approaches +2, corresponding to an oxidation state of 2+. Here, based on the U=4 and 5 eV calculations, the Fe atom donates $4s^2$ electrons to clay. According to Hund's rule, the 2+ and 3+ oxidation states give rise to 4 and 5 μ_B magnetic moments, respectively. Table 1 summarizes the variation of magnetic moment and Bader charge on the Fe atom for the various charged states as well. For a singly charged clay, a magnetic moment of 4.28 μ_B and a Bader charge of 1.89 $|e|$ per Fe were found for U=4 eV, demonstrating a 2+ (Fe^{2+}) oxidation state. The magnetic moment and charge increases slightly for U = 5 eV and HSE06. It is evident that the Hubbard correction with U larger than 4 eV is essential to correctly describe the high-spin oxidation states found in iron-bearing montmorillonite clay via HSE06 calculations[64]. In HSE06 calculations, the charge and magnetic moment on the Fe atom are found to be close to +2 and 4.30 μ_B, respectively.

We compared the energy difference between ferromagnetic (FM) and spin unpolarized (NM) states as a function of the U parameter for the neutral clay. Our calculations show that the energy difference between FM and NM states increases as 0.84→1.11→1.25→1.42→1.74 eV/Fe atom when U varies as 0→1→2→3→4. Figure 2 shows the ferromagnetic and three different antiferromagnetic (AFM) spin configurations, where only the localized d electrons of Fe atoms contribute total magnetic moments. We computed the relative energy of AFM configurations with respect to FM one for U=4 eV. We found that $\Delta E = E_{AFM} - E_{FM}$ is 2, 12 and 23 meV/Fe for AFM1, AFM2 and AFM3, respectively. The FM state has the lowest energy. Due to the large separation between Fe atoms (thereby small exchange interactions), the energy difference between various magnetic states is smaller than k_BT. Therefore, a random spin orientation (paramagnetic state) is likely at room temperature.

Table 1 Magnetic moment (μ_B) and Bader charge on the Fe atom for the neutral, singly, and doubly negatively charged clay slab, calculated using GGA+U (with U=4 and 5) and HSE06 functionals. Lattice parameters, Fe-O, and O-H interatomic distances are also given in Å.

	U=4			U=5			HSE06	
	Neutral	-1e	-2e	Neutral	-1e	-2e	Neutral	-1e
$\mu_{(\mu_B)}$ on Fe	4.08	4.28	4.01	4.27	4.33	3.99	4.30	4.30
Q on Fe	+1.91	+1.89	+1.67	+1.92	+1.92	+1.67	+2.01	+2.01
a (Å)	10.47	10.49	10.49	10.47	10.49	10.49	10.48	10.48
b (Å)	9.02	9.06	9.08	9.04	9.06	9.08	9.04	9.02
$d_{\mathrm{Fe-OH}}$ (Å)	1.99	2.03	2.07	2.01	2.02	2.07	2.00	2.01
$d_{\mathrm{Fe-O}}$ (Å)	1.99-2.02	2.01-2.05	2.05-2.12	2.01-2.02	2.04-2.05	2.05-2.12	2.01-2.02	2.00-2.03
$d_{\mathrm{O-H}}$ (Å)	0.98	0.97	0.97	0.98	0.97	0.97	0.96	0.96

We observed that the extra negative charge is mainly shared between O atoms. This can be seen from Table 1, where the O-H distance decreases as the charge on the slab grows. Since the calculation of binding energies of amino acids on the charged surface brings some technical difficulties and considering the nearly uniform distribution of the extra charge over the clay slab, we utilized a neutral clay slab for the clay-amino acid systems.

3.2 Electronic properties

The electronic properties of the clay surface vary with the charged state and the functional used. Figure 3 denotes the calculated total density of states (DOS) of the whole clay and the projected DOS of Fe d states. It is evident that d states are shifted as the U parameter varies. In general, the Fe 3d states appear inside the band gap of the host material. These d states are shifted towards the conduction band as U grows. For the charged clay, the Fermi level moves toward the conduction band, and the 3d states of Fe merge with the conduction band. The DOS computed with U= 4 and U=5 eV share similar general features with a slightly larger shift of unoccupied d states in U =5 eV. The distribution of occupied and unoccupied d states is quite different when one uses a U value smaller than 2 eV. A comparison of DOS plots obtained with different U values necessitates that HSE06 calculations should be provided to identify the proper U value for the correct description of the electronic properties of the clay slab. For this reason, HSE06 calculations were conducted for the neutral and singly charged clay slab. The first clear observation is that the band gap is significantly enlarged ($\sim$ 7 eV) and the d-states with spin-down character form deep acceptor states within the band gap at least 1.5 eV below the conduction band. For the neutral clay, there is an additional DOS peak around 2 eV originating from p-states of O atoms. Adding an extra charge fills this state. This extra charge is delocalized almost uniformly over the oxygen atoms, which is neutralized by the positive charge from the intercalated sodium cation (Na^+) in multilayer clay. A comparison of HSE06 calculations with those of GGA+U reveals that the band gap values are not predicted correctly with the latter. Nevertheless U $\geq$ 4 eV is appropriate to study clay slab since the main features are reasonably predicted.

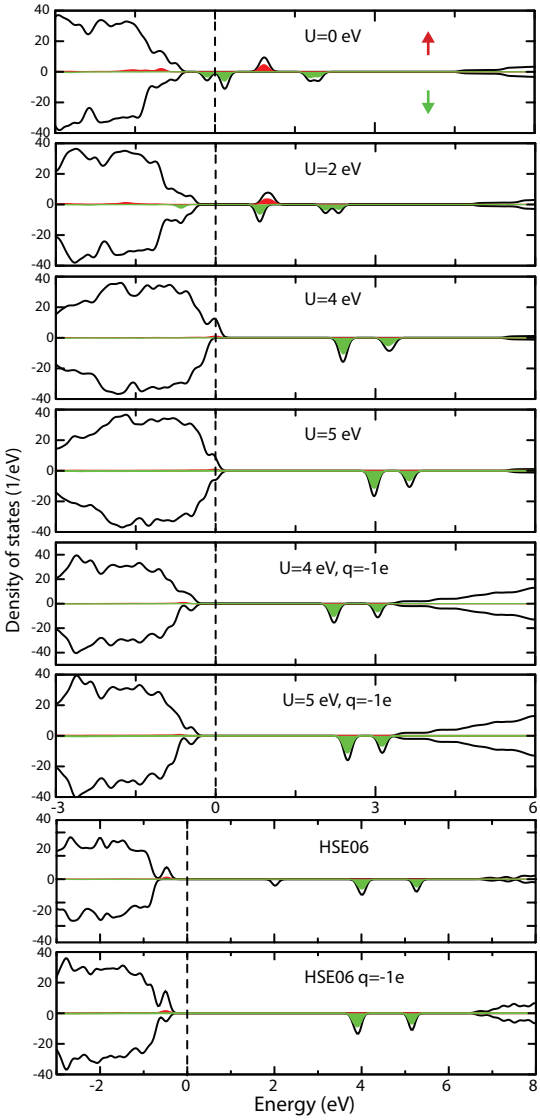

Fig. 3 Density of states for the clay slab for different U values and charge states. Fermi level (vertical black dashed line) is set to zero energy. Red (green) states represent the spin-up (-down) d states of Fe atom. Total DOS is given by black curves.

3.3 Unnatural amino acids

By employing the GGA-PBE functional, we computed the relaxed structures of all unnatural amino acids, as shown in Figure 4.

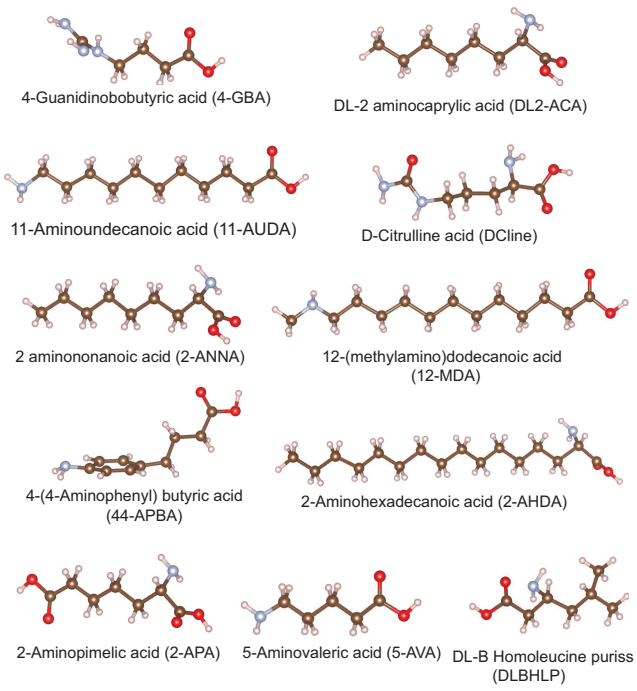

Fig. 4 Relaxed structures of amino acids and the corresponding acronyms depicted in parentheses.

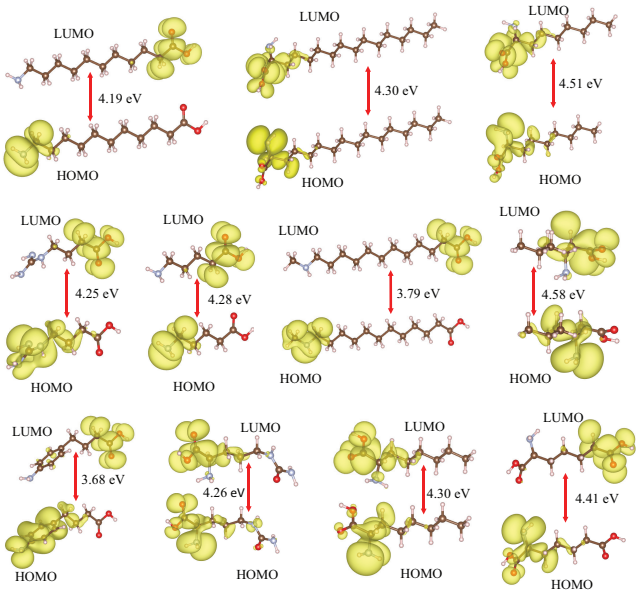

Fig. 5 Charge density of HOMO and LUMO levels of amino acids. HOMO-LUMO gaps are also given.

The charge densities for the highest occupied molecular orbital (HOMO) and lowest unoccupied molecular orbital (LUMO) levels (Figure 5) indicate that the HOMO is predominantly influenced by the amino group (-NH_2), while the LUMO is mainly dominated by the carboxyl group (-COOH). However, the carbon chains exhibit a smaller contribution to these orbitals[28]. The HOMO-LUMO energy gaps range between 3.68 eV and 4.58 eV at the GGA-PBE level of calculations as summarized in Table 2. The dipole moments of the 11 amino acids analyzed in this study, obtained using the PBE and PBE-D3 functionals, exhibit remarkable similarity in both vacuum and solvent environments, except for the molecule DCline, as shown in Figure 6. DCline contains two carbonyl groups with an intervening amine. The incorporation of the D3 correction in PBE enhances the dispersion forces acting on DCline, both in vacuum and solvent environments. As a result, the dipole moments calculated using PBE-D3 align more closely with those obtained from the HSE06 functional, with deviations of 0.29 D and 0.43 D, respectively. Figure 6 also demonstrates that the dipole moment magnitude of the amino acids increases with a higher number of -NH_2 and -COOH groups, both in vacuum and solvent environments.

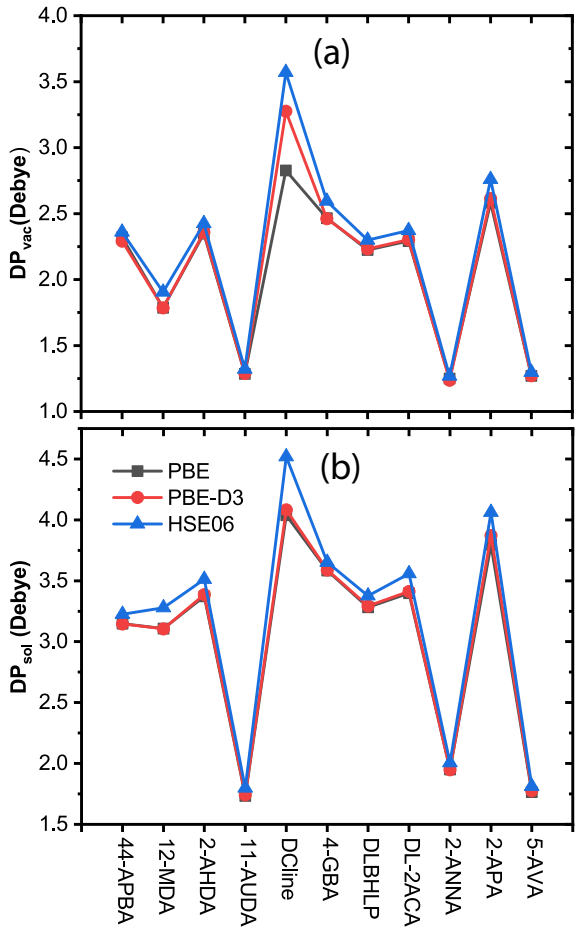

Fig. 6 Total dipole moments in vacuum (DP_{vac}) and in water solvent (DP_{sol}) for each amino acid in Debye (D).

Finally, we also calculated the total energy change per molecule using an implicit water solvent with a dielectric constant of 80. The interaction of amino acid with solvent is correlated with the size of the total dipole moment as shown in Table 2. The dipole moment of amino acids is influenced by the presence of polar regions, such as the -NH_2, -NH and -COOH groups. Amino acids with a larger number of these groups tend to have larger dipole moments. Among the amino acids mentioned, DCline exhibits the largest dipole moment, followed by 2-APA and 4-GBA.

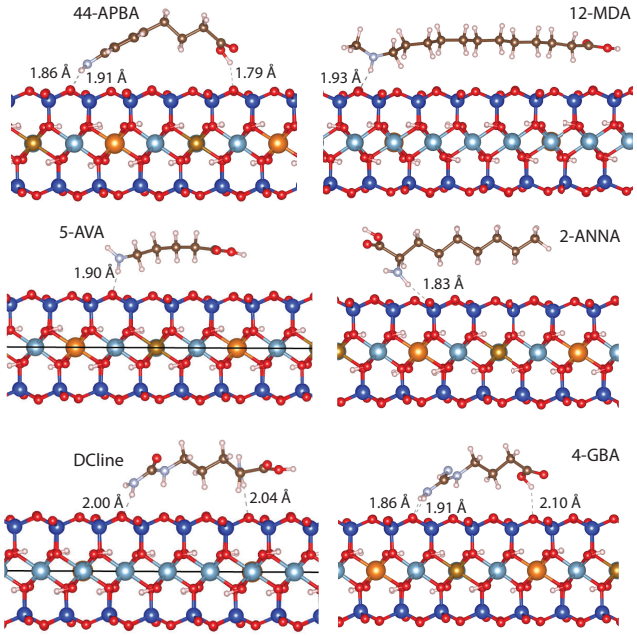

Fig. 7 Lowest energy adsorption structures of the selected amino acids on the clay slab.

3.4 Interaction of the amino acids with the clay surface

Although various studies have been conducted to observe the interactions of amino acids like glycine with clay surfaces[30 32], we used a set of unnatural amino acids in this study as it was indicated in previous sections. These eleven unnatural amino acids were placed on the clay surface to examine their interactions with the clay surface. We considered several adsorption structures of amino acids on the clay surface to find out the lowest energy ones. We performed DFT+U calculations with the U values of 4 and 5 eV, to find the binding energies (E_b^{vac}) of each amino acid molecule. E_b^{vac} was calculated using the following expression; E_b^{vac} (eV/molecule) = E_{tot} (Clay+AA) - E_{tot} (Clay) - E_{tot} (AA), where E_{tot} (Clay) is the total energy of clay, E_{tot} (AA) is the total energy of the amino acid and E_{tot} (Clay+AA) is the total energy of the clay with amino acid adsorbed. Table 2 summarizes the binding energies for the lowest energy adsorption configurations. E_b^{vac} varies between -1.78 to -3.11 eV (for U=4 eV), indicating a strong electrostatic interaction. No chemical bonding between the clay surface and the considered amino acids via charge transfer happens. 44-APBA has the most negative binding energy among the eleven amino acids due to its molecular structure where both -NH_2 and -COOH groups strongly interact with the clay surface. In general, the backbones of the other amino acids are parallel to the clay surface, where the interaction between O of the clay surface and H of the amino acids contribute to the binding. Therefore, 12-MDA, 2-AHDA and 2-AUDA also strongly interact with the clay surface owing to their long backbone, and their binding energies are close to 44-APBA. However, the main contribution to the amino acid binding comes from the -NH_2 group, which is in agreement with results obtained via FT-IR spectra[31], but contrary to another study performed on the adsorption of amino acids on kaolinite surfaces, where the primary role in bonding with the clay surface is played by the -COOH group[65]. The parallel alignment, which is the lowest energy alignment, on the surface significantly affects the contribution of -the COOH group on binding. For instance, even though DCline amino acid has two -NH, one -NH_2, and one -COOH group, its binding energy is about 0.6 eV less than 44-APBA.

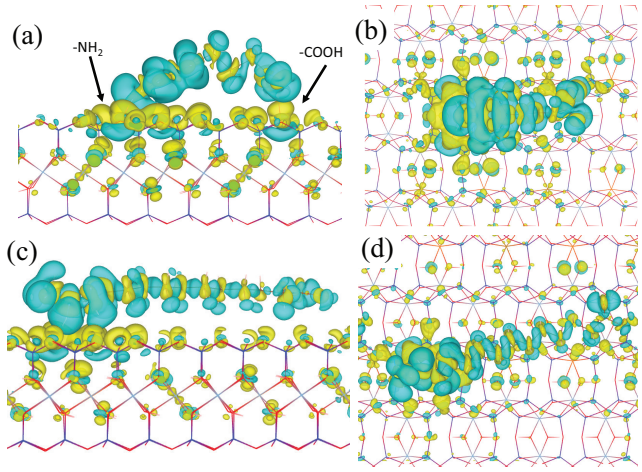

Fig. 8 Charge density difference for 44-APBA (side view in (a) and top view in (b)) and 12-MDA (side view in (c) and top view in (d)) on the clay surface. The accumulation of electrons is represented by cyan color while the electron depletion is shown by yellow.

Figure 8 is an illustration of the charge density difference for the 44-APBA and 12-MDA adsorbed on the clay surface. The charge density difference is calculated using the following equation; $\rho(\text{Diff}) = \rho(\text{clay}-\text{AA}) - \rho(\text{clay}) - \rho(\text{AA})$, where $\rho(\text{clay}+\text{AA})$, $\rho(\text{clay})$ and $\rho(\text{AA})$ are the charge densities for the clay + amino acid, clay and amino acid, respectively. When the charge density distribution is concerned, it is evident that the adsorption of the amino acid molecules does not affect the opposite side of the clay surface, and the effect decays when moving away from the molecule, since the interactions are only effective at the particular region of surface where the molecule is placed on. The clay-amino acid interaction is accompanied by a significant change in the charge density of the -NH_2 and surface oxygen atoms of the clay surface being near the -NH_2 group. Figure 8 suggests that -NH_2 dominates the bonding process as compared to the -COOH group and the backbone of the amino acids, as pointed out above. The impact of the carboxyl groups on the interaction with the clay slab is two-folded. As the surface of the slab is negatively charged, the oxygen atoms of the carboxyl group prefer to stay away from the surface to avoid repulsion from the surface. It contributes to binding via an attractive O-H interaction, where O is a surface atom. We also calculated E_b^{vac} for U =5 eV. We found that E_b^{vac} calculated with U= 4 eV and 5 eV are quite similar. Slight differences may be due to the local relaxation effects.

Table 2 HOMO-LUMO (H-L_{vac} in eV) gap of amino acids in vacuum. ΔE_{sol}^{vac} represents the interaction energy of amino acid with water solvent. It is the difference in the total energy of amino acid in vacuum and solvent. E_b^{vac} and E_b^{sol} are the calculated binding energies of amino acids on the clay surface for vacuum and water solvent. Energies are given in eV/amino acid.

Amino Acid	H-L_{vac}	ΔE_{sol}^{vac}	E_b^{vac} (U=4 eV)	E_b^{vac} (U=5 eV)	E_b^{sol} (U=4 eV)
44-APBA	3.68	0.54	-3.11	-3.18	-4.47
12-MDA	3.79	0.34	-2.91	-2.99	
2-AHDA	4.30	0.33	-2.62	-2.66	
11-AUDA	4.19	0.40	-2.42	-2.45	
DCline	4.26	0.95	-2.48	-2.55	-3.64
4-GBA	4.25	0.74	-2.31	-2.39	
DLBHLP	4.58	0.43	-1.92	-1.96	
DL-2ACA	4.30	0.38	-1.82	-1.84	
2-ANNA	4.51	0.35	-1.81	-1.86	
2-APA	4.41	0.75	-2.06	-2.10	
5-AVA	4.28	0.43	-1.78	-1.79	-2.63

3.5 Effect of an implicit solvent on the adsorption of molecules

We investigated the effect of an implicit solvent on the clay-amino acid systems for U=4 eV. The solvent that was used here was water (H_2O). Previous studies have demonstrated that the addition of water favors the adsorption of amino acids on both MMT and kaolinite clay surfaces[66]. The implicit representation of the solvent, which is the type we used here, is an approximation to the explicit one which is more accurate than the former. However, for calculating binding energies of amino acid molecules on the clay surface, we would need to consider many H_2O molecules and configurations of those molecules and take an average over these configurations, which is computationally very expensive[67–69]. Therefore, we preferred to use the implicit model. Total energies of eleven amino acids and clay when the solvent is present were calculated, and it was compared with the values obtained when the solvent was absent. In order to comprehend the influence of the solvent on the bond lengths and structures of molecules, we thoroughly reoptimized the molecular configurations. As shown in Table 2, the lowest (0.327 eV) and the highest (0.945 eV) energy difference were obtained for 2-AHDA and DCline molecules, respectively. DCline has multiple amino groups, which strengthen its interaction with the solvent. For the clay slab, the energy difference between relaxed clay with and without solvent is found to be 0.988 eV. Next, we calculated the binding energies of some of these molecules with the clay surface and the results depict that the binding energy increases with the addition of the water solvent.

3.6 Molecular dynamic simulations

We performed ab-initio molecular dynamic (AIMD) simulations in vacuum for the selected systems to assess the stability of the clay-amino acid system at a finite temperature. We simulated a canonical ensemble where a Nose-Hoover thermostat was employed. We tracked the variation of energy and structural parameters as a function of simulation time. Figure 9 shows the energy variation over about 7.5 ps simulation time for 44-APBA, 5-AVA, and 12-MDA, where the total energy oscillates around an average value at 300 K, and no sharp variation is observed. All three

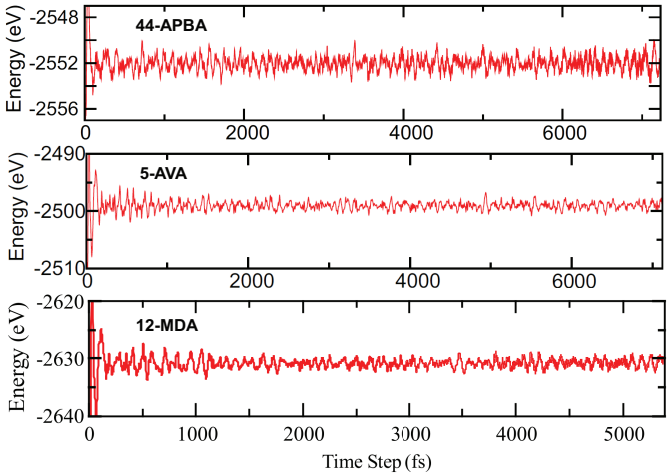

Fig. 9 Molecular dynamics simulations for clay-44-APBA, clay-5-AVA and clay-12-MDA systems. Variation of total energy as a function of time step at 300K is given.

amino acids remain bound to the clay surface without any change in binding configuration. Figure 10 shows the snapshots of clay 44-APBA at various time steps. It is evident the amino acid wiggles on the clay surface with small instant changes in interatomic lengths between amino acid and clay atoms.

4 Conclusions

In summary, this ab-initio study using density functional theory focused on investigating the structural, electronic, and magnetic properties of iron and magnesium co-doped montmorillonite clay, along with its interaction with eleven unnatural amino acid molecules for the development of novel bio-material composites. We employed various DFT functionals, including PBE-GGA, PBE-GGA+U, and HSE06, to assess their impact on clay properties. Our findings highlighted the necessity of using GGA+U with $U \geq 4$ eV or HSE06 to accurately model the electronic behavior of iron. Regarding the bare amino acids, the HOMO level was mainly influenced by the amino (-NH_2) group, while the LUMO level was dominated by the carboxyl (-COOH) group. An uncharged clay slab was utilized for the adsorption of amino acids,

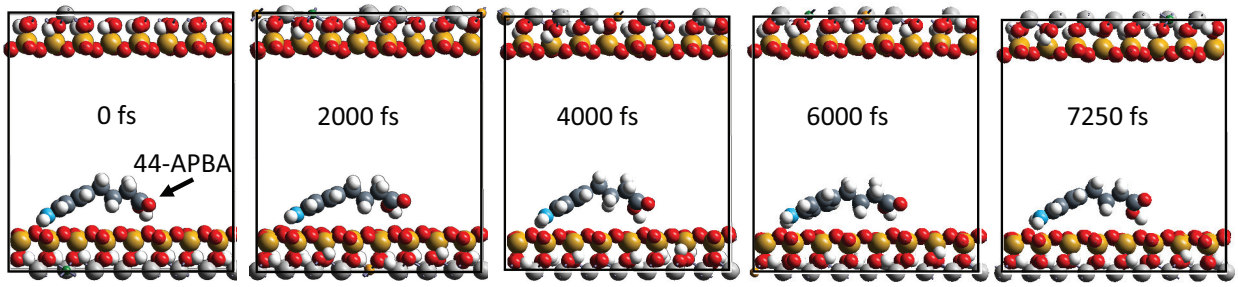

Fig. 10 Evolution of the binding structure of 44-APBA on the clay surface as a function of simulation time.

and DFT+U calculations were performed to determine binding energies. We observed binding energies ranging from -1.78 to -3.11 eV, suggesting a strong electrostatic interaction without any charge transfer or sharing. The 44-APBA molecule exhibited particularly strong binding due to its unique structure, which allows the binding of both amino and carboxyl groups on the clay surface. Further analysis with an implicit H_2O solvent revealed enhanced binding energies. Finally, molecular dynamics simulations were conducted for selected molecules, indicating stable binding with the clay surface at 300 K, with no significant variations in energy, structural parameters, or binding structures over time.

Conflicts of interest

There are no conflicts to declare.

Disclosure statement

Any opinions, findings, and conclusions, or recommendations expressed in this material are those of the author(s) and do not necessarily reflect the views of the National Science Foundation.

Acknowledgements

This material is based upon work supported by the National Science Foundation under grant OIA-1946202. All computations were carried out at NDSU CCAST, which is supported by NSF grants 1229316 and 2019077.

Notes and references

1 G. S. Travlos, *Toxicologic Pathology*, 2006, **34**, 548–565.
2 M. Ansari, *Progress in Biomaterials*, 2019, **8**, 223–237.
3 L. Ambrosio, M. G. Raucci, G. VadalÃ , L. Ambrosio, R. Papalia and V. Denaro, *Innovative Biomaterials for the Treatment of Bone Cancer*, 2021, https://doi.org/10.3390/ijms22158214.
4 P. Chocholata, V. Kulda and V. Babuska, *Materials*, 2019, **12**, year.
5 R. Dimitriou, E. Jones, D. McGonagle and P. V. Giannoudis, *BMC Medicine*, 2011, **9**, 66.
6 T. G. Kim, H. Shin and D. W. Lim, *Advanced Functional Materials*, 2012, **22**, 2446–2468.
7 B. Pei, W. Wang, Y. Fan, X. Wang, F. Watari and X. Li, *Regenerative Biomaterials*, 2017, **4**, 257–268.
8 G. Turnbull, J. Clarke, F. Picard, P. Riches, L. Jia, F. Han, B. Li and W. Shu, *Bioactive Materials*, 2018, **3**, 278–314.
9 L. Bedian, A. M. Villalba-Rodríguez, G. Hernández-Vargas, R. Parra-Saldivar and H. M. Iqbal, *International Journal of Biological Macromolecules*, 2017, **98**, 837–846.
10 K. Haraguchi and H.-J. Li, *Macromolecules*, 2006, **39**, 1898–1905.
11 A. Usuki, N. Hasegawa, M. Kato and S. Kobayashi, in *Polymer-Clay Nanocomposites*, Springer Berlin Heidelberg, Berlin, Heidelberg, 2005, pp. 135–195.
12 H. W. P. Carvalho, C. V. Santilli, V. Briois and S. H. Pulcinelli, *RSC Adv.*, 2013, **3**, 22830–22833.
13 Y. Cui, S. Kumar, B. Rao Kona and D. van Houcke, *RSC Adv.*, 2015, **5**, 63669–63690.
14 A. J. Bur, Y.-H. Lee, S. C. Roth and P. R. Start, *Polymer*, 2005, **46**, 10908–10918.
15 J. K. Pandey, K. Raghunatha Reddy, A. Pratheep Kumar and R. Singh, *Polymer Degradation and Stability*, 2005, **88**, 234–250.
16 S. Wang, L. Shen, Y. Tong, L. Chen, I. Phang, P. Lim and T. Liu, *Polymer Degradation and Stability*, 2005, **90**, 123–131.
17 D. Sikdar, S. M. Pradhan, D. R. Katti, K. S. Katti and B. Mohanty, *Langmuir*, 2008, **24**, 5599–5607.
18 A. H. Ambre, D. R. Katti and K. S. Katti, *Journal of Biomedical Materials Research Part A*, 2013, **101A**, 2644–2660.
19 A. Ambre, K. S. Katti and D. R. Katti, *Materials Science and Engineering: C*, 2011, **31**, 1017–1029.
20 A. H. Ambre, K. S. Katti and D. R. Katti, *Journal of Nanotechnology in Engineering and Medicine*, 2010, **1**, year.
21 C. Zhou, D. Tong and W. Yu, in *7 - Smectite Nanomaterials: Preparation, Properties, and Functional Applications*, Elsevier, 2019, pp. 335–364.
22 S. Ghazanfari, H. N. Faisal, K. S. Katti, D. R. Katti and W. Xia, *Langmuir*, 2022, **38**, 4859–4869.
23 S. Ghazanfari, Y. Han, W. Xia and D. S. Kilin, *The Journal of Physical Chemistry Letters*, 2022, **13**, 4257–4262.
24 C. R. Ferreira, S. H. Pulcinelli, L. Scolfaro and P. D. Borges, *ACS Omega*, 2019, **4**, 14369–14377.
25 L. Fu and H. Yang, *Nanoscale Research Letters*, 2017, **12**, 411.
26 V. V. T. Padil, K. P. Akshay Kumar, S. Murugesan, R. Torres-Mendieta, S. Waclawek, J. Y. Cheong, M. Cernik and R. S. Varma, *Green Chemistry*, 2022, **24**, 3081–3114.
27 R. K. Math, N. Bharatham, P. K. Javaregowda and H. D. Yun, *Applied Microscopy*, 2021, **51**, 17.

28 J. N. Nkoh, Z. Hong, H. Lu, J. Li and R. Xu, *Applied Clay Science*, 2022, **219**, 106437.

29 T. Dashman and G. Stotzky, *Soil Biology and Biochemistry*, 1982, **14**, 447–456.

30 C. Zhu, Q. Wang, X. Huang, J. Yun, Q. Hu and G. Yang, *Colloids and Surfaces B: Biointerfaces*, 2019, **183**, 110458.

31 L. Benetoli, C. De Souza, K. Silva, I. Junior, H. de Santana, A. Jr Paesano, A. Costa, C. Zaia and D. Zaia, *Origins of life and evolution of the biosphere : the journal of the International Society for the Study of the Origin of Life*, 2008, **37**, 479–93.

32 E. Escamilla-Roa, F. Huertas, A. Hernandez-Laguna and C. Sainz-Diaz, *Phys. Chem. Chem. Phys.*, 2017, **19**, year.

33 N. Kumari and C. Mohan, in *Basics of Clay Minerals and Their Characteristic Properties*, ed. G. M. D. Nascimento, IntechOpen, Rijeka, 2021, p. Ch. 2.

34 K. Krol-Morkisz and K. Pielichowska, in *13 - Thermal Decomposition of Polymer Nanocomposites With Functionalized Nanoparticles*, Elsevier, 2019, pp. 405–435.

35 Z. Chen, W. Zhang, M. Wang, L. J. Backman and J. Chen, *ACS Biomaterials Science & Engineering*, 2022, **8**, 2321–2335.

36 W. Qiao, D. Pan, Y. Zheng, S. Wu, X. Liu, Z. Chen, M. Wan, S. Feng, K. M. C. Cheung, K. W. K. Yeung and X. Cao, *Nature Communications*, 2022, **13**, 535.

37 P. Hohenberg and W. Kohn, *Phys. Rev.*, 1964, **136**, B864–B871.

38 W. Kohn and L. J. Sham, *Phys. Rev.*, 1965, **140**, A1133–A1138.

39 G. Kresse and J. Furthmuller, *Phys. Rev. B*, 1996, **54**, 11169–11186.

40 G. Kresse and J. Furthmüller, *Computational Materials Science*, 1996, **6**, 15–50.

41 G. Kresse and J. Hafner, *Phys. Rev. B*, 1993, **47**, 558–561.

42 P. E. Blochl, *Phys. Rev. B*, 1994, **50**, 17953–17979.

43 G. Kresse and D. Joubert, *Phys. Rev. B*, 1999, **59**, 1758–1775.

44 J. P. Perdew, K. Burke and M. Ernzerhof, *Phys. Rev. Lett.*, 1996, **77**, 3865–3868.

45 V. I. Anisimov, J. Zaanen and O. K. Andersen, *Phys. Rev. B*, 1991, **44**, 943–954.

46 N. Mosey, P. Liao and E. Carter, *The Journal of chemical physics*, 2008, **129**, 014103.

47 J. Heyd and G. Scuseria, *J. Chem. Phys.*, 2003, **118**, year.

48 J. Heyd and G. Scuseria, *The Journal of chemical physics*, 2004, **121**, 1187–92.

49 D. Richard and N. M. Rendtorff, *Applied Clay Science*, 2021, **213**, 106251.

50 C. R. Luna, W. G. Reimers, M. J. Avena and A. Juan, *Phys. Chem. Chem. Phys.*, 2021, **23**, 14601–14607.

51 W. Tang, E. Sanville and G. Henkelman, *Journal of Physics: Condensed Matter*, 2009, **21**, 084204.

52 E. Sanville, S. D. Kenny, R. Smith and G. Henkelman, *Journal of Computational Chemistry*, 2007, **28**, 899–908.

53 *Computational Materials Science*, 2006, **36**, 354–360.

54 M. Yu and D. R. Trinkle, *The Journal of Chemical Physics*, 2011, **134**, 064111.

55 K. Mathew, R. Sundararaman, K. Letchworth-Weaver, T. Arias and R. G. Hennig, *The Journal of chemical physics*, 2014, **140**, 084106.

56 K. Mathew, V. C. Kolluru, S. Mula, S. N. Steinmann and R. G. Hennig, *The Journal of Chemical Physics*, 2019, **151**, 234101.

57 H. J. Monkhorst and J. D. Pack, *Phys. Rev. B*, 1976, **13**, 5188–5192.

58 S. Grimme, J. Antony, S. Ehrlich and H. Krieg, *The Journal of chemical physics*, 2010, **132**, 154104.

59 E. Johnson and A. Becke, *The Journal of chemical physics*, 2006, **124**, 174104.

60 D. J. Evans and B. L. Holian, *The Journal of chemical physics*, 1985, **83**, 4069–4074.

61 A. Hassan, M. Ismail, A. H. Reshak, Z. Zada, A. A. Khan, F. U. R. M, M. Arif, K. Siraj, S. Zada, G. Murtaza and M. M. Ramli, *Journal of Molecular Structure*, 2023, **1274**, 134484.

62 M. J. Frisch, G. W. Trucks, H. B. Schlegel, G. E. Scuseria, M. A. Robb, J. R. Cheeseman, G. Scalmani, V. Barone, B. Mennucci, G. A. Petersson, H. Nakatsuji, M. Caricato, X. Li, H. P. Hratchian, A. F. Izmaylov, J. Bloino, G. Zheng, J. L. Sonnenberg, M. Hada, M. Ehara, K. Toyota, R. Fukuda, J. Hasegawa, M. Ishida, T. Nakajima, Y. Honda, O. Kitao, H. Nakai, T. Vreven, J. J. A. Montgomery, J. E. Peralta, F. Ogliaro, M. Bearpark, J. J. Heyd, E. Brothers, K. N. Kudin, V. N. Staroverov, R. Kobayashi, J. Normand, K. Raghavachari, A. Rendell, J. C. Burant, S. S. Iyengar, J. Tomasi, M. Cossi, N. Rega, J. M. Millam, M. Klene, J. E. Knox, J. B. Cross, V. Bakken, C. Adamo, J. Jaramillo, R. Gomperts, R. E. Stratmann, O. Yazyev, A. J. Austin, R. Cammi, C. Pomelli, J. W. Ochterski, R. L. Martin, K. Morokuma, V. G. Zakrzewski, G. A. Voth, P. Salvador, J. J. Dannenberg, S. Dapprich, A. D. Daniels, Farkas, J. B. Foresman, J. V. Ortiz, J. Cioslowski and D. J. Fox, *Gaussian 09 (Gaussian, Inc., Wallingford CT)*, Wallingford, CT, 2009.

63 J. Zhao, Y. Cao, L. Wang, H.-J. Zhang and M.-C. He, *Minerals*, 2021, **11**, year.

64 G. Rollmann, A. Rohrbach, P. Entel and J. Hafner, *Phys. Rev. B*, 2004, **69**, 165107.

65 A. Kasprzhitskii, G. Lazorenko, D. S. Kharytonau, M. A. Osipenko, A. A. Kasach and I. I. Kurilo, *Applied Clay Science*, 2022, **226**, 106566.

66 J. I. Hedges and P. E. Hare, *Geochimica et Cosmochimica Acta*, 1987, **51**, 255–259.

67 S. N. Steinmann, P. Sautet and C. Michel, *Physical Chemistry Chemical Physics*, 2016, **18**, 31850–31861.

68 M. Saleheen and A. Heyden, *ACS Catalysis*, 2018, **8**, 2188–2194.

69 T. Xie, S. Sarupria and R. B. Getman, *Molecular Simulation*, 2017, **43**, 370–378.